Criteria for Cross-Plane Dominated Thermal Transport in Multilayer Thin Film Systems During Modulated Laser Heating[1]

Patrick E. Hopkins[2]
e-mail: pehopki@sandia.gov

Justin R. Serrano

Leslie M. Phinney
ASME Fellow

Sean P. Kearney

Thomas W. Grasser

C. Thomas Harris[3]

Engineering Sciences Center,
Sandia National Laboratories,
P.O. Box 5800,
Albuquerque, NM 87185-0346

Pump-probe transient thermoreflectance (TTR) techniques are powerful tools for measuring the thermophysical properties of thin films, such as thermal conductivity, Λ, or thermal boundary conductance, G. This paper examines the assumption of one-dimensional heating on, Λ and G, determination in nanostructures using a pump-probe transient thermoreflectance technique. The traditionally used one-dimensional and axially symmetric cylindrical conduction models for thermal transport are reviewed. To test the assumptions of the thermal models, experimental data from Al films on bulk substrates (Si and glass) are taken with the TTR technique. This analysis is extended to thin film multilayer structures. The results show that at 11 MHz modulation frequency, thermal transport is indeed one dimensional. Error among the various models arises due to pulse accumulation and not accounting for residual heating. [DOI: 10.1115/1.4000993]

1 Introduction

Pump-probe transient thermoreflectance (TTR) techniques utilizing short pulsed lasers have been extensively used to measure thermal conductivity, Λ, and thermal boundary conductance, G, of nanomaterials and interfaces of nanomaterials, such as Λ in metal films [1], dielectric films [2], phase change materials [3], thermally anisotropic materials [4], superlattice structures [5], and layered nanolaminates [6,7], and G across metal-metal [8], metal-dielectric [9–13], and metal-liquid [14] interfaces. These transient thermoreflectance techniques measure the change in reflectance on the surface of a material as a function of time after a short pulsed heating event. The change in reflectance is related to the temperature change in the electrons in the material, and the measured change in temperature as a function of time is then related to Λ and G through a conduction heat equation.

Although the aforementioned Λ and G measurements use similar pump-probe time delayed TTR setups, there have been different assumptions regarding the heat transfer analyses in several of the studies; for example, for measurements of G at metal film/dielectric substrate interfaces, two different thermal analyses have been used for the same basic experimental conditions [12,13]. This paper examines the effects of different thermal analyses on determination of cross-plane Λ and G from TTR measurements on thin film samples by comparing one-dimensional and axisymmetric cylindrical models for thermal transport in TTR measurements. The models are fitted to TTR experimental data on Al/Si and

Al/glass systems and extended to TTR data with thin Pt, SiO$_2$, and SiN$_x$ films; the thermal properties of which are extremely important in both microfabricated structures and microelectromechanical systems (MEMS).

The experiments and analyses in this work are focused on pulsed laser heating from a Ti:sapphire oscillator with a fundamental output of 90 fs pulses at 80 MHz (12.5 ns between laser pulses); the laser pulses are then further modulated at 11 MHz to create a modulated heating event at the sample surface, and the temperature decay on the surface of the samples from this modulated heating events is monitored over ~ 4 ns. The laser pulses are treated as delta functions in time due to the ultrashort pulse width compared with the time delay of the experiments. The thermal penetration depth of the modulated heat source is estimated by $\sqrt{D/(\pi f)}$, where D is the diffusivity and f is the modulation frequency. For most solids subjected to megahertz thermal modulation rates, the thermal penetration depth is anywhere from 100 nm to 10 μm. To ensure mostly cross-plane (one-dimensional) transport, the laser spot size of the modulated heating source should be greater than the thermal penetration depth. Typical TTR experiments utilize pump spot sizes on the order of 10 μm. Therefore, for low diffusivity systems, the thermal transport measured in TTR experiments is nearly entirely cross plane due to the small thermal penetration depth. However, in high thermal diffusivity systems, in-plane thermal transport can become significant. The goal of this work is to determine when cross-plane transport is dominant in TTR experiments in various thin film systems. The regimes in which cross-plane transport dominate TTR measurements are discussed in more quantitative detail in the remainder of this work through the use of various thermal models and the development of a nondimensional number describing relative contributions of in-plane and cross-plane thermal transports.

2 Thermal Analysis

2.1 One-Dimensional Time-Domain Model. A one-dimensional heat transfer model for heat transfer between two conductive solids was used by several groups to determine G at several film/substrate interfaces [9–11,13]. This model is given by

---

$$C_{1,2}\frac{\partial \theta_{1,2}(z,t)}{\partial t} = \Lambda_{1,2}\frac{\partial^2 \theta_{1,2}(z,t)}{\theta z^2} \qquad (1)$$

which describes heat conduction in the film (subscript 1) or substrate (subscript 2), where C is the volumetric heat capacity, θ is the temperature change due to the laser pulse, t is the time after the laser pulse, and z is the direction of heat flow. Since typical laser pulse widths in TTR experiments are on the order of hundreds of femtoseconds yet the measurements of G at the film/substrate interface and Λ in the underlying substrate are resolved on the order of nanoseconds, the heating event is assumed to be instantaneous and the initial conditions governing Eq. (1) are

$$\theta_1(z,0) = \frac{Q}{C_1 \xi \pi w_0^2}\exp[-z/\xi] \qquad (2)$$

and

$$\theta_2(z,0) = 0 \qquad (3)$$

where Q is the absorbed energy from the incident heating event (pump pulse), ξ is the energy deposition depth in the film, w_0 is the pump $1/e^2$ radius, and Eq. (3) imposes the semi-infinite substrate assumption. The energy deposition depth is given by $\xi = \lambda/(4\pi n_2)$ where λ is the laser pulse wavelength and n_2 is the extinction coefficient (imaginary component of the complex index of refraction) of the solid in which the laser pulse is interacting. In TTR experiments, placing a metal film on top of the material to be characterized ensures that the majority of the laser pulse energy is absorbed near the surface of the film. Since TTR experiments give a spatial resolution no less than ξ, this ensures resolution on the order of 10 nm. For example, the extinction coefficient for Al at 785 nm is 8.55 [15], yielding an energy penetration depth (and subsequent TTR resolution) of 7.3 nm. The boundary conditions at the film/substrate interface (that is, when z is equal to the film thickness d) governing Eq. (1) are given by

$$-\Lambda_{1,2}\frac{\partial \theta_{1,2}(d,t)}{\partial z} = G_{12}(\theta_1(d,t) - \theta_2(d,t)) \qquad (4)$$

For purposes in this work, Eqs. (1)–(4) are called the one-dimensional time-domain model (1Dt). The 1Dt is solved using a Crank–Nicolson scheme to determine $\theta(t)$ at the surface of the film. Any analysis based on the 1Dt model assumes only one-dimensional transport and no effect from lateral heat spreading.

2.2 Axially Symmetric Frequency-Domain Model. In typical TTR experiments, the pump and probe beams have spatially Gaussian intensity distributions when incident on the film surface. Therefore, depending on the relative sizes and overlap of the beams, the radial distributions of the pump beam could affect the temperature measured by the probe beam. In this case, the 1Dt may not be applicable since it assumes that the probe reflectance, or the measured change in temperature, is measuring a uniformly heated plane at the surface of the film. To correct for this, Cahill [16] derived an expression for $\theta(r)$ at the surface of the film assuming radial spreading in a half-sphere from the pump pulse. Here we rederive Cahill's expression in a more general fashion.

The axially symmetric heat equation in cylindrical coordinates is given by

$$C_1\frac{\partial \theta_1(r,z,t)}{\partial t} = \Lambda_{1,z}\frac{\partial^2 \theta_1(r,z,t)}{\partial z^2} + \frac{\Lambda_{1,r}}{r}\frac{\partial}{\partial r}\left(r\frac{\partial \theta_1(r,z,t)}{\partial r}\right) \qquad (5)$$

where r is the radial coordinate, and the subscripts r and z denote the radial and cross-plane conductivities. Taking the Hankel transform along the radial, planar dimension, then applying a Fourier transform, Eq. (5) leads to

$$\frac{\partial^2 \theta_1(r,z,\omega)}{\partial z^2} = q_1^2 \theta_1(r,z,\omega) \qquad (6)$$

where ω is the angular frequency and

$$q^2 = \frac{\Lambda_r k^2 + iC\omega}{\Lambda_z} \qquad (7)$$

where k is the transform variable. This anisotropic q was used by Schmidt et al. [4] to determine the directionally dependent thermal conductivities of graphite in anisotropic structures. In this work, however, we consider isotropic materials and we are only interested in cross-plane properties, so $q^2 = k^2 + (iC\omega/\Lambda_z)$.

The temperature change in the surface of the film due to heat flow through underlying materials is easily taken into account through Carslaw and Jaeger's solution for steady periodic temperature change in composite slabs [17]. A convenient implementation of this is presented by Feldman [18] and discussed here. The change in surface temperature of material 1 is given by

$$F(k) = \frac{1}{\gamma_1}\left(\frac{F_{T1}^+ + F_{T1}^-}{F_{T1}^- - F_{T1}^+}\right) \qquad (8)$$

where F_{T1}^+ and F_{T1}^- are temperature change coefficients related to the forward and backward propagating waves on the surface (top side) of material 1 and where $\gamma = \Lambda_z q$. The forward and backward propagating waves at the top side of material 1 are related to the waves on the bottom side through

$$\begin{bmatrix} F_{T1}^+ \\ F_{T1}^- \end{bmatrix} = \begin{bmatrix} \exp[-q_1 d_1] & 0 \\ 0 & \exp[q_1 d_1] \end{bmatrix}\begin{bmatrix} F_{B1}^+ \\ F_{B1}^- \end{bmatrix} \qquad (9)$$

where d is the material thickness. For material 1, the top side is assumed at the slab/air interface and the bottom side is assumed as the interface between material 1 and material 2 (i.e., film/substrate). Given a thermal boundary conductance G between material 1 and material 2, the temperature at the top of slab 2 is related to the temperature at the bottom side of slab 1 by

$$\begin{bmatrix} F_{B1}^+ \\ F_{B1}^- \end{bmatrix} = \frac{1}{2}\begin{bmatrix} 1 + \dfrac{\gamma_2}{\gamma_1} - \dfrac{\gamma_2}{G_{12}} & 1 - \dfrac{\gamma_2}{\gamma_1} + \dfrac{\gamma_2}{G_{12}} \\ 1 - \dfrac{\gamma_2}{\gamma_1} - \dfrac{\gamma_2}{G_{12}} & 1 + \dfrac{\gamma_2}{\gamma_1} + \dfrac{\gamma_2}{G_{12}} \end{bmatrix}\begin{bmatrix} F_{T2}^+ \\ F_{T2}^- \end{bmatrix} \qquad (10)$$

Assuming a bulk substrate, heat cannot reach the bottom side of slab 2 at rates comparable to the modulation frequency (semi-infinite), so there is no thermal buildup of waves and

$$\begin{bmatrix} F_{T2}^+ \\ F_{T2}^- \end{bmatrix} = \begin{bmatrix} 0 \\ \exp[-q_2 d_2] \end{bmatrix} \qquad (11)$$

With Eqs. (9)–(11), this approach gives a straightforward method to solve for heat conduction through several materials and interfaces via successive implementation of Eqs. (9) and (10) for each layer and then Eq. (11) for the final, semi-infinite layer. This is much less computationally expensive than solving the 1Dt for each interface and material.

To determine the temperature oscillations on the surface of material 1 with the frequency-domain model in Eq. (6) due to cooling from underlying layers described by Eqs. (9)–(11), a top surface boundary condition must be imposed. In TTR, this is described by first convoluting Eq. (8) with the pump-beam distribution [4], given by

$$\theta(k) = F(k)\frac{A}{2\pi}\exp\left[\frac{-k^2 w_0^2}{8}\right] \qquad (12)$$

and then taking the weighted average of the surface temperature oscillations by the probe beam of $1/e^2$ radius w_1 [16] to yield

$$\theta(r,0,\omega) = \frac{A}{2\pi}\int_0^\infty F(k)\exp\left[\frac{-k^2(w_0^2 + w_1^2)}{8}\right]k\,dk \qquad (13)$$

Equation (13) gives the change in temperature as a function of heating event modulation frequency at the surface of the film. In this paper, Eq. (13) is called the axially symmetric frequency-domain model (Axf). The Axf has been used by several groups to

determine G [12,19] and, due to its simple extension to multilayer structures, the thermal conductivity of thin layers and multilayered structures [2,6,7,20–22]. Note that, in this development, the pump source is assumed to be applied only at the surface, so substrate effects on the pump distribution are nonexistent. Although Eq. (13) accounts for radial effects in TTR, it does not give the response as a function of time, which is measured in TTR. To examine the temporal evolution of Eq. (13), the response of the material systems to the laser and modulation repetition rates must be considered. This is described in detail in Sec. 2.3.

2.3 Laser Modulation and Thermal Accumulation Effects. Due to the relatively small change in voltage due to the probe thermoreflectance response as compared with the dc voltage from the reflected probe, a lock-in amplifier is used in the TTR data collection to monitor the temporal decay in the thermoreflectance response occurring at the modulation frequency of the heating event. The output of the lock-in amplifier serves to relate frequency-domain models to the time-domain. The lock-in output will be the magnitude R and phase ϕ of the probe signal at the heating event modulation frequency. Mathematically, the lock-in output takes the form of [4]

$$R \exp[i(\omega_0 t + \phi)] = Z(\omega_0)\exp[i\omega_0 t] \qquad (14)$$

where ω_0 is the modulation frequency of the pump pulses and $Z(\omega_0)$ is the transfer function of the lock-in. In the frequency-domain, the transfer function can be represented as [16]

$$Z(\omega_0) = \frac{(2\pi)^2\chi}{\omega_s^2} \sum_{M=-\infty}^{\infty} \theta(\omega_0 + M\omega_s)\exp[iM\omega_s\tau] \qquad (15)$$

where θ is calculated with a frequency-domain model, such as the model discussed in Sec. 2.2, ω_s is the modulation frequency of the laser system (not the modulation frequency of the heating event; so for a Ti:Al_2O_3 oscillator, $\omega_s/2\pi$ is approximately 80 MHz), τ is the delay time between the pump and probe pulses, and χ is a constant that is related to the gain of the electronics, the power of the pump and probe pulses, and the thermoreflectance coefficient of the material. The thermoreflectance coefficient, which relates the change in temperature from the model to the change in reflectance measured in the experiment, is a material property that is related to the band structure, electronic transitions, and dielectric function [23]. In the low perturbation regime (i.e., small temperature rise of the film compared with ambient) in which this work is focused, the change in reflectance is linearly related to the change in temperature, and the thermoreflectance coefficient is a constant. We account for the thermoreflectance coefficient by normalizing the data to the model, as discussed in Sec. 3. From Eq. (15), the lock-in outputs are given by

$$X = \text{Re}[Z(\omega_0)], \quad Y = \text{Im}[Z(\omega_0)] \qquad (16)$$

where X and Y are the real and imaginary components of the measured frequency response, and

$$R = \sqrt{X^2 + Y^2}, \quad \phi = \tan^{-1}\left[\frac{Y}{X}\right] \qquad (17)$$

By nature of Eq. (15), pulse-to-pulse heating and thermal accumulation due to pump modulation are taken into account with a frequency-domain model (note that, in this work, when calculating temporal response with the frequency-domain models, such as the Axf, it is implied that the frequency-domain models are used in conjunction with Eq. (15) to determine the time-domain response). Although a similar model can be derived for pulse accumulation in the time-domain [4], it has not been used in works using a 1Dt analysis, most likely due to the numerical cost, which negates the benefit of using the simplified model in the time-domain. Even with exact analytical forms of the conduction thermal diffusion equation obtained by Laplace transforms [24], accounting for pulse accumulation can be computationally expen-
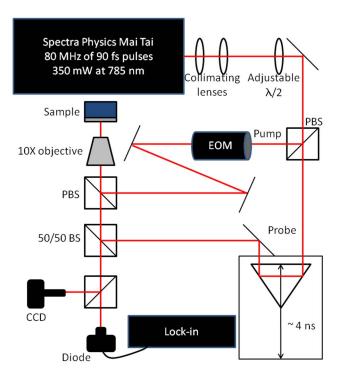

Fig. 1 Transient thermoreflectance setup at Sandia National Laboratories

sive compared with that in the frequency-domain since, in the time-domain, the solution must take into account the multiple pulses in the pump modulation envelope occurring every 12.5 ns while providing picosecond resolution in the analysis.

3 Experimental Details

The various thermal models discussed in Sec. 2 are applied to data for determining G and Λ from pump-probe measurements using the transient thermoreflectance experimental setup at Sandia National Laboratories. The experimental setup, shown in Fig. 1, is nearly identical to similar setups that exploit coaxial pump-probe geometries discussed in previous works [4,25,26]. The laser pulses in this specific experimental setup emanate from a Spectra Physics Mai Tai oscillator outputting 350 mW of power at a repetition rate of 80 MHz and pulse widths of 90 fs at a wavelength of 785 nm. The setup shown in Fig. 1 differs from previous collinear setups by two slight modifications. First, the pulses are first passed through a pair of collimating lenses to minimize probe divergence at the sample surface due to the variable delay stage; upon characterization with a sweeping knife edge [27], the probe (and pump) radius at minimum pump-probe delay is ~15 μm and exhibits less than 1 μm divergence at maximum delay. Then, the pulse train passes through an adjustable half-waveplate before being split into the pump and probe paths by a polarizing beam splitter (PBS) cube; this fixes the pump and probe path as orthogonally polarized and the waveplate therefore allows for easy adjustment of the pump and probe powers; the relative pump and probe powers are adjusted to achieve a maximum thermoreflectance signal.

The data must be postprocessed to remove any electronic noise that would lead to unwanted signals. These signals would appear as a change in the imaginary component of the signal Y, as τ crosses zero, since Y should not change as the pump-probe delay time goes from negative to positive. Schmidt et al. [4] determined the change in the real and imaginary components of the signals and calculated a phase noise to subtract from the data. Cahill [16] corrected for this by multiplying the signal by a small phase factor. Here, we employ the following correction: The change in the
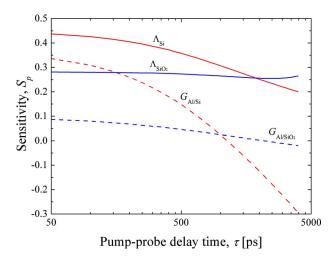
Fig. 2 Sensitivities of the Axf to G and Λ of the substrate in 100 nm Al/Si and Al/SiO₂ systems

Table 1 Thermophysical properties of Al, Si, and SiO₂ at 300 K [31]

	Λ (W m^{-1} K^{-1})	C (MJ m^{-3} K^{-1})
Al	237	2.44
Si	148	1.66
SiO₂	1.4	1.97

lock-in signals as the delay time crosses $\tau=0$, ΔX, and ΔY are computed from the collected data. The measured signals are corrected by rotating the signal in the complex plane, so that the corrected values for X and Y are given by [28]

$$X_c = X \cos\left[\tan^{-1}\left[\frac{\Delta Y}{\Delta X}\right]\right] - Y \sin\left[\tan^{-1}\left[\frac{\Delta Y}{\Delta X}\right]\right] \quad (18)$$

and

$$Y_c = Y \cos\left[\tan^{-1}\left[\frac{\Delta Y}{\Delta X}\right]\right] + X \sin\left[\tan^{-1}\left[\frac{\Delta Y}{\Delta X}\right]\right] \quad (19)$$

A similar method of data correction was employed by Costescu et al. [19] to correct the data for radial diffusion in the substrate. In practice, the phase of the lock-in is adjusted before each measurements so that Y is constant as the stage moves across $\tau=0$ [16] so that Eqs. (18) and (19) can be used simply as a check to ensure that the phase adjustment has removed the majority of the instrument noise. This also allows for the instrument noise to be quantified in terms of the lock-in phase so that this adjustment can be used in future measurements and analysis [29].

To evaluate the various thermophysical properties of interest, we must determine an appropriate range in which to fit the various models to the experimental data. For example, a given material system may be extremely sensitive to changes in G over a certain range but not Λ. This aspect of the models is used to determine ranges in which to fit the various models to the data. Costescu et al. [19] defined a sensitivity factor as

$$S_p = \partial \ln\left[-\frac{X}{Y}\right] \Big/ \partial \ln[p] \quad (20)$$

where p is some thermophysical property of interest. To determine the sensitivity of G or Λ over the pump-probe delay time in the TTR data, we perturb the value of G or Λ by 1% in calculations of Eq. (20) so effectively our sensitivity becomes

$$S_p = 100 \frac{Y}{X} \partial\left[\frac{X}{Y}\right] \quad (21)$$

where the derivative of the ratio is estimated by subtracting the model calculations from the perturbed model calculations. Figure 2 shows the sensitivities of the Axf as a function of pump-probe delay time for a 100 nm Al film on Si and SiO₂ substrates using the thermal parameters in Table 1 and assuming a 15 μm pump and probe spot size with an absorbed laser power of 1 mW. In the sensitivity calculations, the thermal boundary conductances are taken as 100 MW m^{-2} K^{-1} for Al/Si [13] and 50 MW m^{-2} K^{-1} for Al/SiO₂ [30]. There are two aspects of the sensitivity curve

that are important when fitting the model to the TTR data: the magnitude and the curvature. An optimal sensitivity curve will exhibit a large magnitude and variance over the pump-probe delay time. For example, the sensitivity to the thermal conductivity of the Si substrate is ideal since it is relatively large and very dynamic compared with that of SiO₂. The sensitivity to G across the Al/Si interface is also appealing but loses sensitivity around 500–1000 ps. Note that the sensitivity of the model in the Al/SiO₂ system is primarily due to the thermal conductivity of the substrate. For low thermal conductivity structures, this is powerful if only the thermal conductivity needs to be determined and not G since it reduces the number of free parameters in the fit. We do not include the sensitivity to the Al film thermal conductivity since the TTR measurements are nearly insensitive to this parameter over the majority of the pump-probe time delay. Assuming a diffusivity of Al as $D=97.1\times10^{-6}$ m^2 s^{-1}, the time it takes for the heat to diffuse through the film is given by $\tau\approx d^2/D$ where d is the film thickness [31]. For a 100 nm Al film, the thermal energy has fully diffused through the film thickness after only 100 ps.

TTR data on a 100 nm Al film evaporated onto a single crystalline, lightly doped Si substrate and a glass microscope cover slide (primarily SiO₂) are shown in Fig. 3 along with Axf and 1Dt model calculations. The thermal conductivity of the 100 nm Al film is 200 W m^{-1} K^{-1} as determined from electrical resistivity measurements and the Wiedemann–Franz law. Although this procedure for determining the Al thermal conductivity is really a
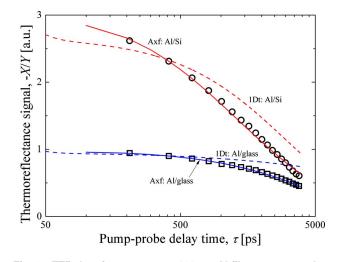

Fig. 3 TTR data from scans on 100 nm Al films evaporated on Si (circles) and glass (squares) substrates along with the best fit from the Axf model scaled at 400 ps. Using the best fit values of G and Λ_2 from the Axf, the 1Dt is calculated and scaled to the data showing that the 1Dt fails to capture some aspects of the data. The thermophysical properties determined from Axf model best fits are $G=90$ MW m^{-2} K^{-1} for the Al/Si interface, $\Lambda=142$ W m^{-1} K^{-1} for Si, and $G=40$ MW m^{-2} K^{-1} and $\Lambda=1.0$ W m^{-1} K^{-1} for the glass substrate. The measured thermal conductivity of the glass substrate is lower than that of pure SiO₂ since the substrate in this case is a glass microscope slide, so the various impurities will reduce the thermal conductivity below that of pure SiO₂.

measure of in-plane conductivity where the model requires cross plane, since the Al film is amorphous, it is valid to assume that the in-plane and cross-plane conductivities are equivalent for a 100 nm Al film. The Axf model, which is assumed here as the more precise model since it takes into account pulse accumulation and radial spreading, is scaled at 400 ps and G_{12} and Λ_2 are adjusted to determine the best fit. Using the best fit values from the Axf, the 1Dt is calculated and scaled to the data in Fig. 3. The data shown here are the real component of the lock-in signal divided by the imaginary component, i.e., $-X/Y$. This approach of normalizing the signal by the imaginary component of the voltage cancels out detection noise and makes the signal insensitive to various experimental parameters that can be difficult to account for during data analysis [16]. This approach is the same as using the phase of the signal [4,14]. Note that we also scale the models to the data at some time t. We choose 400 ps as the scale time since any nonequilibrium phenomena in the Al film have equilibrated and thermal diffusion in the Al film is negligible compared with the diffusion across the Al/substrate interface and in the substrate. The advantage of scaling the model to the data is that precise values for spot sizes or absorbed laser power are no longer needed. However, these inputs are critical if the transport is not purely 1D, and if radial transport plays a role in the TTR measurements, then precise values for spot sizes must be known. However, as will be shown in later sections, 1D transport can be assumed in many cases, which significantly simplifies data analysis.

In Fig. 3, the 1Dt model and the data do not exhibit great agreement in trends. Since we assume that the Axf is the more precise model, the 1Dt fails to predict the thermophysical properties of interest in TTR at 11 MHz modulation frequency. Therefore, the question is as follows: Why does the 1Dt fail? There are two major differences between the 1Dt and Axf. One is the effect of pulse accumulation from the repetition rate of the pump pulses. This aspect on thermal analyses of TTR data has been extensively studied previously and will not be repeated here. However, in short, it must be taken into account analytically in the thermal models (i.e., Sec. 2.3) [4], or the data must be corrected by accounting for the pump-phase [27]. In the remainder of this work, we will focus on the dimensionality assumption in TTR experiments; that is, we will answer the following question: When does radial transport need to be considered in TTR analyses?

4 One-Dimensional Versus Axially Symmetric Transport

The most straightforward way to compare the effects of radial transport on G and Λ is to replace the Axf model presented in Sec. 2.2 with a one-dimensional model. The heat equation in one-dimensional Cartesian coordinates is given by Eq. (6) only

$$q^2 = \frac{iC\omega}{\Lambda_z} \tag{22}$$

The temperature is given by

$$F(\omega) = \frac{1}{\gamma_1}\left(\frac{F_{T1}^+ + F_{T1}^-}{F_{T1}^- - F_{T1}^+}\right) \tag{23}$$

where the various coefficients are evaluated based on the algorithm outlined in Sec. 2.2. Note that Eq. (22) is in the frequency-domain and not in the time-domain. Since no radial heating is assumed, no convolution of the frequency response and the pump pulse is necessary. Therefore, the temperature change due to pump heating is given by

$$\theta(\omega) = F(\omega)\frac{A}{\pi w_0^2} \tag{24}$$

However, we are interested in only the fraction of the temperature change measured by the probe beam, so the measured temperature change is
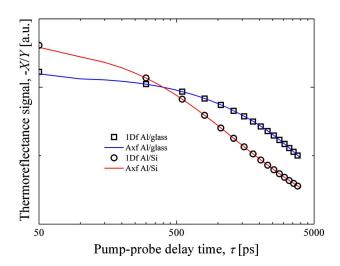

Fig. 4   Comparison of 1Df and Axf for a 100 nm Al film on a Si and glass substrate using the material properties determined from the fit in Fig. 3. The 1Dt and Axf are identical for these two material systems.

$$\theta(\omega) = F(\omega)\frac{Aw_1^2}{\pi w_0^4} \tag{25}$$

Note if $w_0 = w_1$, Eq. (25) reduces to Eq. (24).

Using Eq. (25) with the analyses in Sec. 2.2 (multilayer analysis, Eqs. (9)–(11)) and Sec. 2.3 (modulation analysis, Eqs. (15) and (16)), a one-dimensional frequency-domain model (1Df) is obtained. The 1Df and Axf for the Al/Si and Al/SiO$_2$ systems in Fig. 3 are compared in Fig. 4. The calculations of the Axf and 1Df are identical for the Al/Si and Al/SiO$_2$ systems over the delay times of interest. In addition, the 1Df fit to the data and best fits that are determined to those found using the Axf (see Fig. 3 caption). This means that the discrepancy between the models shown in Fig. 3 is due to pulse accumulation and not dimensionality. This is intuitive, since the only difference between the development of the 1Dt and the 1Df is the analysis that accounts for the modulated heating event and pulse accumulation, and therefore, given purely cross-plane thermal transport, the 1Dt and 1Df will only differ if pulse-to-pulse residual heating cannot be ignored; this aspect of pulse accumulation is treated in detail by Schmidt et al. [4]. Therefore, a 1D assumption is appropriate for thermal analyses of TTR data on film/substrate systems at modulation frequencies of 11 MHz. This ensures that at 11 MHz the cross-plane properties of material systems are measured.

5 Condition for One-Dimensional Transport

To examine the regimes where one-dimensional, cross-plane transport dominates the thermal processes, we calculate the ratio of the 1Df signal to the Axf signal as a function of heating event modulation frequency. We define the signals as the ratio of the real to imaginary temperature rises predicted from the models, $-T_{Re}/T_{Im}$. This parallels the ratio of lock-in signals previously discussed—i.e., $-X/Y$. Figure 5 shows the predictions of the ratio of the 1Df to Axf signals assuming a 15 μm probe spot radius. Figure 5(a) shows the calculations assuming a 1:1 pump/probe radius ratio (i.e., 15 μm pump radius) and Fig. 5(b) shows results assuming a 5:1 ratio (i.e., 75 μm pump radius). We consider modulation frequencies that are typical in TTR experiments—10 kHz–20 MHz. For these simulations, we assume an 100 nm Al film on a semi-infinite substrate with various thermal diffusivities, $D = \Lambda/C$ as indicated in the figure, and a constant thermal boundary conductance of 50 MW m^{-2} K^{-1}. The Al thermal properties are assumed as bulk and listed in Table 1.
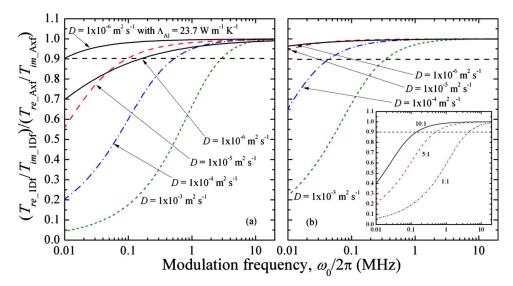
Fig. 5 Ratio of the 1Df signal to the Axf signal as a function of heating event modulation frequency where the signals are defined as the ratio of the real to imaginary temperature rises predicted from the models, $-T_{\text{Re}}/T_{\text{Im}}$. An acceptable range to assume one-dimensional cross-plane transport is defined as when the 1Df signal ratio is within 90% of the Axf signal ratio as indicated by the horizontal dashed line. (a) Calculations assuming a 1:1 pump/probe radius ratio (i.e., 15 μm pump radius) shows that one-dimensional transport is achieved at modulation frequencies above 500 kHz except when the substrate material has diffusivities comparable to that of diamond ($D \sim 1 \times 10^{-3}$ m^2 s^{-1}), in which case radial transport must be taken into account at modulation frequencies as high as 2 MHz. (b) Calculations assuming a 5:1 ratio (i.e., 75 μm pump radius). Radial heating is less apparent as the pump spot size increases. The inset of (b) shows the 1Df/Axf ratio for an 100 nm Al film on graphite for three pump-probe spot size ratios—10:1, 5:1, and 1:1.

We define an "acceptable" range to assume one-dimensional cross-plane transport when the 1Df signal ratio is within 90% of the Axf signal ratio; this factor is indicated in Fig. 5 by the horizontal dashed line. When considering the same pump and probe spot sizes (Fig. 5(a)), one-dimensional transport is achieved at modulation frequencies above 500 kHz except when the substrate material has diffusivities comparable to that of diamond ($D \sim 1 \times 10^{-3}$ m^2 s^{-1}), in which case radial transport must be taken into account at modulation frequencies as high as 2 MHz. An interesting aspect of dimensionality in transport is observed in the lowest diffusivity calculations (diffusivities comparable to SiO$_2$, ($D \sim 1 \times 10^{-6}$ m^2 s^{-1})). As the diffusivity of the substrate decreases from that comparable to diamond, the trends in the comparative ratio follow similar patterns; lower diffusivities mean one-dimensional transport can be assumed, and the curvature as a function of frequency follows similar trends. However, in low diffusivity substrates, the curvature as a function of frequency does not resemble that of the other diffusivity curves. This is due to the fact that as frequency decreases the thermal penetration depth becomes smaller, such that the density of heat deposited in the Al film is larger. In a nonconducting substrate, radial diffusion in the conducting Al film spreads heat much more quickly than in the substrate, so that the effect of radial spreading in the Al film affects the dimensionality of the heat flow in the film substrate system as more heat is deposited in the Al film (i.e., as the thermal penetration depth decreases). To test this analysis, we repeat these same calculations assuming that the Al film has a thermal conductivity that is 10% of bulk, and, as shown in Fig. 5(a), the trends follow those of the higher diffusivity substrates. This could lend insight into a unique experimental study in which to determine the in-plane thermal conductivity of thin-metal films. Figure 5(b) shows the same calculations in Fig. 5(a) only assuming a 5:1 pump-to-probe spot size ratio. As expected, the effect of radial heating is less severe as the pump spot size increases. This leads to a general

conceptual conclusion that to ensure purely one-dimensional thermal transport, the heating event should be modulated at high frequencies and deposited over a large area (heat deposited in system should resemble a short, fat cylinder). The inset of Fig. 5(b) shows the 1Df/Axf ratio for an 100 nm Al film on graphite, a highly anisotropic system in which radial measurements were recently performed with TTR by Schmidt et al. [4]. For the graphite calculations, we assume $\Lambda_z = 5.7$ W m^{-1} K^{-1}, $\Lambda_r = 1950$ W m^{-1} K^{-1}, $C = 1.56$ MW m^{-2} K^{-1}, and $G_{\text{Al/graphite}} = 50$ MW m^{-2} K^{-1} [4,31]. The calculations are performed for three pump-probe spot size ratios—10:1, 5:1, and 1:1. In graphite, the effects of radial heating become apparent at higher modulation frequencies than in isotropic structures, which is intuitive since the in-plane (radial) direction is much more conductive than the cross-plane direction.

Using this conceptual conclusion, we define a nondimensional number H to determine when one-dimensional heating can be assumed, given by

$$H = \frac{w_0 + \ell_r}{\ell_z} \tag{26}$$

where w_0 is the radius of the heating event, ℓ_r is the distance the heat travels in the radial direction (i.e., an effective thermal spreading distance), and ℓ_z is the thermal penetration depth in the cross-plane direction. Where the cross-plane thermal penetration depth is defined as $\ell_z = \sqrt{2D_z/\omega_0}$, the thermal spreading distance can be derived to take a similar form as $\ell_r = \sqrt{2D_r/\omega_0}$ where D_r is the diffusivity in the radial direction. To ensure one-dimensional thermal transport, $H \gg 1$. For an isotropic material, the condition for one-dimensional transport is
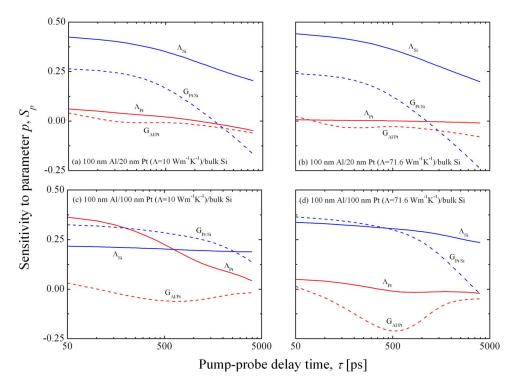
$$H = \frac{w_0}{\ell} \gg 1 \tag{27}$$

Fig. 6 Sensitivities of the Axf as a function of pump-probe delay time for four different Pt films of varying thickness and thermal conductivity. The various conductivities assumed for the Pt films are listed in the figures. Other parameters used for these calculations are $G_{Al/Pt}$ =500 MW m^{-2} K^{-1}, C_{Pt}=2.85 MJ m^{-3} K^{-1}, and $G_{Pt/Si}$=140 MW m^{-2} K^{-1}. The properties used for the Al film and bulk Si substrate are listed in Table 1.

As previously discussed and following from Eq. (27), to ensure one-dimensional transport, a large heating spot size and a small thermal penetration depth (high frequency) are desired.

6 Multilayer Films

To test the effects of radial conduction on thermal conductivity measurements in thin films, we grew and deposited a series of thin-metal and dielectric films (75 nm Pt, 51 nm SiO$_2$, 46 nm SiN$_x$, and 232 nm SiN$_x$ films) on polished Si [100] substrates with 1 Ω cm resistivity, capped with an 80 nm film of Al for our TTR transducer layer. All metal films were deposited using electron beam evaporation, with the Pt metal film requiring a 3 nm chromium adhesion layer. Before the Pt deposition, the Si substrate was subjected to a dilute hydrofluoric acid (HF) dip. The SiO$_2$ film consisted of a dry thermal oxide, and the low pressure chemical vapor deposition (LPCVD) SiN$_x$ films were deposited in a low-stress (100 MPa) state. A standard RCA clean was performed on the Si substrates before the growth and deposition of the SiO$_2$ and SiN$_x$ films.

Before measuring the thermal properties of these film systems, we analyze the sensitivity of the models to the various thermal boundary conductances and thermal conductivities that will be driving the TTR signal using Eq. (21). Figure 6 shows the measurement sensitivities of the Axf to the various thermal conductances in the Al/Pt/Si sample. Although the Pt sample is 75 nm, since the conductivity is unknown, we model four different scenarios to show the range of sensitivities: (a) 20 nm Pt film with Λ=10 W m^{-1} K^{-1}, (b) 20 nm Pt film with Λ=71.6 W m^{-1} K^{-1}, (c) 100 nm Pt film with Λ=10 W m^{-1} K^{-1}, and (d) 100 nm Pt film with Λ=71.6 W m^{-1} K^{-1}. In the thinner Pt film cases ((a) and (b)), the sensitivity to the thermal conductivity is small, with a nearly zero sensitivity to the Pt thermal conductivity in the high conductivity case. In this case, the thermal signal will be dominated by G at the Pt/Si interface and Λ_{Si}. As the thickness of the Pt film is increased, the sensitivity to the thermal conductivity of

the film increases. In addition, as the film conductivity decreases, the sensitivity increases. This is intuitive since a thicker, less conductive film will offer more thermal resistance.

Where the Pt thin film is relatively thermally conductive, the SiN$_x$ and SiO$_2$ films are expected to be substantially less conductive. Therefore, the sensitivity of the TTR signal to a nonconductive film is shown in Fig. 7. The thermal response is still relatively sensitive to the underlying Si substrate thermal conductivity for a 50 nm SiO$_2$ film and also sensitive to the SiO$_2$/Si thermal boundary conductance, as seen in Fig. 7(a). However, increasing the thickness of the SiO$_2$ film to 250 nm causes the thermal response to be completely insensitive to the properties of the substrate (Fig. 7(b)). For comparison, Fig. 7(c) shows the thermal response when the 250 nm SiO$_2$ film is replaced with a conductive Pt film of the same thickness. Note that the thermal signal becomes very sensitive to the Si interfacial conductance and conductivity since the Pt film offers very little resistance to the thermal circuit.

TTR data on these samples were taken at 11 MHz pump modulation frequency; a summary of the TTR fitting results is summarized in Table 2. For the Pt system, since the thermal measurement is relatively insensitive to the Pt conductivity, we estimate Λ_{Pt} from electrical resistivity measurements as 40.5 W m^{-1} K^{-1}. Note that any errors in the Pt thermal conductivity do not propagate into the other reported results on this system since the measurement is relatively insensitive to Λ_{Pt} with conductivity of this order of magnitude (see Fig. 6). We take $G_{Pt/Si}$ as 140 MW m^{-2} K^{-1} [13] leaving $G_{Al/Pt}$ as the only free parameter that we determine as 290 MW m^{-2} K^{-1}. This result is quite surprising as the measured G at the Al/Pt interface is approximately the same as those measured at Al/semiconductor interfaces [13] and over an order of magnitude less than the conductance measured at Al–Cu metal-metal interfaces. The reduction in the measured $G_{Pt/Si}$ from the previously measured $G_{Al/Cu}$ [8] could be due to the band structures of the two metals comprising each interface. Both Al and Cu are free electron metals, and the electrons in the
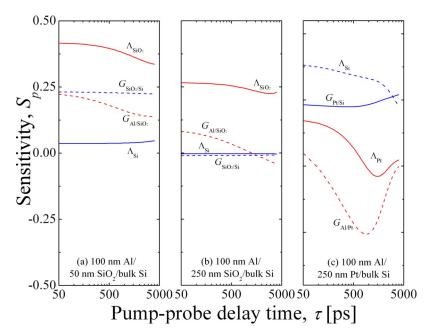
Fig. 7 Sensitivities of the Axf as a function of pump-probe delay time for two SiO$_2$ films with thicknesses of (*a*) 50 nm and (*b*) 250 nm. The thermal response with these insulative films is relatively insensitive to the thermal conductivity of the substrate over the pump-probe delay time. For comparison, the sensitivity of using a conductive Pt film of 250 nm is shown in (*c*). The thermal properties for the 250 nm Pt film are assumed bulk (see Fig. 5), and the other parameters assumed for these calculations were $G_{Al/Pt}$=500 MW m^{-2} K^{-1}, C_{Pt} =2.85 MJ m^{-3} K^{-1} , and $G_{Pt/Si}$=140 MW m^{-2} K^{-1}.

parabolic conduction bands contribute to thermal conduction. These relatively low effective masses of the electrons lead to low electrical resistivities, and so the thermal boundary conductance between the low electrically resistive free electron metal will be large. However, Pt is much more electrically resistive than copper, and it has a complicated band structure with relatively flat *d*-bands overlapping the Fermi surface. Although the low electrical resistivity of the Pt will reduce $G_{Al/Pt}$ to below that of $G_{Al/Cu}$, the presence of *s*-band electrons in Al interacting with *d*-band electrons in Pt can cause phonon emission for momentum conservation leading to an additional electron-phonon resistance that would decrease $G_{Al/Pt}$ to values similar to $G_{Pt/Si}$.

The TTR signals of the three other thin film samples (51 nm SiO$_2$, 46 nm SiN$_x$, and 232 nm SiN$_x$) are primarily dominated by the thermal conductivity of the film. The heat capacity for SiN$_x$ used in the fit is C_{SiN_x}=1.65 MJ m^{-3} K^{-1} [31]. The thermal conductivity of the 232 nm SiN$_x$ film was measured as 3.5 W m^{-1} K^{-1}, with G_{Al/SiN_x} as 110 MW m^{-2} K^{-1}. Using this value for G_{Al/SiN_x} in the fit of the 46 nm SiN$_x$ film, we determine the thermal conductivity of the 46 nm SiN$_x$ film as 3.1 W m^{-1} K^{-1} with $G_{SiN_x/Si}$ as 50 MW m^{-1} K^{-1}. Finally, we determine the thermal conductivity of the SiO$_2$ film as 1.2 W m^{-1} K^{-1}, with G_{Al/SiO_2} as 100 MW m^{-1} K^{-1} and $G_{SiO_2/Si}$ as 20 MW m^{-1} K^{-1}. The values for thermal conductivity of the

thin dielectric films are slightly higher than previously reported measurements [30], which is expected due to the higher quality of the films in this study. In addition, the values for thermal boundary conductance agree well with previously reported values for metal/dielectric interfaces, but are lower for the dielectric/dielectric interface conductances [30,32].

All properties determined from TTR fits with the Axf were also fitted with the 1Df to determine the effect of dimensionality. In all scenarios in this work, the Axf and 1Df yielded the exact same result, indicating that the thermal transport was completely 1D (cross plane). This is expected for these samples since the pump modulation frequency is 11 MHz and the thermal response is almost entirely cross plane, as apparent from the analysis in Sec. 5 (see Fig. 5). At the high pump modulation frequency used in this work (11 MHz), the thermal penetration depth is relatively small; the multilayer samples measured in this section yield *H* ∼ 10–100 ≫ 1, which ensures that the TTR measurements are probing the cross-plane transport. A lower modulation frequency would lead to a larger penetration depth, which could lead to significant radial heating depending on the spot size [4].

7 Conclusions

This paper examines the assumption of one-dimensional heating and pulse accumulation on *G* and Λ determination in nanostructures using a pump-probe transient thermoreflectance technique. The traditionally used one-dimensional and axially symmetric cylindrical conduction models are reviewed in Sec. 2, along with the lock-in response that takes into account pulse accumulation and residual heating. To test the assumptions of the models, experimental data of Al films on bulk substrates (Si and glass) are taken with the TTR technique described in Sec. 3. The sensitivity of the Axf to the various thermophysical parameters is discussed in Sec. 4, along with the fitting algorithm and assumptions. To determine the error associated with assuming one-dimensional thermal transport, the Axf is compared with a one-

Table 2 TTR measurements on multilayer thin film samples

	G_{12} (MW m^{-2} K^{-1})	Λ_2 (W m^{-1} K^{-1})	G_{23} (MW m^{-2} K^{-1})
Al/75 nm Pt/Si	290 ± 150	40.5	140
Al/232 nm SiN$_x$/Si	110	3.5 ± 0.2	-
Al/46 nm SiN$_x$/Si	110	3.1 ± 0.1	50 ± 2.8
Al/51 nm SiO$_2$/Si	100	1.2 ± .1	20 ± 4.0

dimensional frequency-domain model. This analysis is extended to thin film multilayer structures. Results show that at 11 MHz modulation frequency, thermal transport is indeed one dimensional. Error among the various models arises due to pulse accumulation and not accounting for residual heating.

Acknowledgment

Nomenclature

A = power absorbed at the sample surface, W
C = heat capacity, $J\ m^{-3}\ K^{-1}$
D = thermal diffusivity, $m^2\ s^{-1}$
d = film thickness, m
F = change in temperature in Hankel space, K
G = thermal boundary conductance, $W\ m^{-2}\ K^{-1}$
H = nondimensional number to determine when thermal transport is primarily one dimensional
J_0 = zeroth order Bessel function
k = transform variable, m^{-1}
ℓ = thermal penetration depth, m
M = index in frequency-domain representation of lock-in transfer function
m = index in time-domain representation of lock-in transfer function
n_2 = extinction coefficient
p = thermophysical property of interest
Q = energy per pulse, J
R = magnitude of lock-in signal
r = direction radial to sample surface, m
S = sensitivity
t = time, s
t_m = heating event time, s
w = $1/e^2$ laser spot radius, m
X = real component of lock-in frequency response
Y = imaginary component of lock-in frequency response
z = direction normal to the sample surface, m

Greek Symbols

δ = change in
χ = proportionality constant in lock-in transfer function
θ = measured change in temperature, K
Λ = thermal conductivity, $W\ m^{-1}\ K^{-1}$
λ = laser wavelength, m
ϕ = phase of lock-in signal
ω = angular frequency, $rad\ s^{-1}$
ξ = optical penetration depth, m
τ = pump-probe delay time, s

Subscripts

0 = pump
1 = layer 1 (top layer/metal film)
2 = layer 2
12 = from layer 1 to layer 2
B = bottom
c = corrected for electronic noise
Im = imaginary
p = probe
r = radial
Re = real
s = laser system
T = top
z = cross plane

References

[1] Paddock, C. A., and Eesley, G. L., 1986, "Transient Thermoreflectance From Thin Metal Films," J. Appl. Phys., **60**, pp. 285–290.
[2] Koh, Y. K., and Cahill, D. G., 2007, "Frequency Dependence of the Thermal Conductivity of Semiconductor Alloys," Phys. Rev. B, **76**, p. 075207.
[3] Lyeo, H.-K., Cahill, D. G., Lee, B.-S., and Abelson, J. R., 2006, "Thermal Conductivity of Phase-Change Material Ge$_2$Sb$_2$Te$_5$," Appl. Phys. Lett., **89**, p. 151904.
[4] Schmidt, A. J., Chen, X., and Chen, G., 2008, "Pulse Accumulation, Radial Heat Conduction, and Anisotropic Thermal Conductivity in Pump-Probe Transient Thermoreflectance," Rev. Sci. Instrum., **79**, p. 114902.
[5] Capinski, W. S., Maris, H. J., Ruf, T., Cardona, M., Ploog, K., and Katzer, D. S., 1999, "Thermal-Conductivity Measurements of GaAs/AlAs Superlattices Using a Picosecond Optical Pump-and-Probe Technique," Phys. Rev. B, **59**, pp. 8105–8113.
[6] Chiritescu, C., Cahill, D. G., Nguyen, N., Johnson, D., Bodapati, A., Keblinski, P., and Zschack, P., 2007, "Ultralow Thermal Conductivity in Disordered, Layered WSe$_2$ Crystals," Science, **315**, pp. 351–353.
[7] Costescu, R. M., Cahill, D. G., Fabreguette, F. H., Sechrist, Z. A., and George, S. M., 2004, "Ultra-Low Thermal Conductivity in W/Al$_2$O$_3$ Nanolaminates," Science, **303**, pp. 989–990.
[8] Gundrum, B. C., Cahill, D. G., and Averback, R. S., 2005, "Thermal Conductance of Metal-Metal Interfaces," Phys. Rev. B, **72**, p. 245426.
[9] Hopkins, P. E., Norris, P. M., Stevens, R. J., Beechem, T., and Graham, S., 2008, "Influence of Interfacial Mixing on Thermal Boundary Conductance Across a Chromium/Silicon Interface," ASME J. Heat Transfer, **130**, p. 062402.
[10] Hopkins, P. E., Stevens, R. J., and Norris, P. M., 2008, "Influence of Inelastic Scattering at Metal-Dielectric Interfaces," ASME J. Heat Transfer, **130**, p. 022401.
[11] Stoner, R. J., and Maris, H. J., 1993, "Kapitza Conductance and Heat Flow Between Solids at Temperatures From 50 to 300 K," Phys. Rev. B, **48**, pp. 16373–16387.
[12] Lyeo, H.-K., and Cahill, D. G., 2006, "Thermal Conductance of Interfaces Between Highly Dissimilar Materials," Phys. Rev. B, **73**, p. 144301.
[13] Stevens, R. J., Smith, A. N., and Norris, P. M., 2005, "Measurement of Thermal Boundary Conductance of a Series of Metal-Dielectric Interfaces by the Transient Thermoreflectance Technique," ASME J. Heat Transfer, **127**, pp. 315–322.
[14] Schmidt, A., Chiesa, M., Chen, X., and Chen, G., 2008, "An Optical Pump-Probe Technique for Measuring the Thermal Conductivity of Liquids," Rev. Sci. Instrum., **79**, p. 064902.
[15] Palik, E. D., 1985, *Handbook of Optical Constants of Solids*, Academic, Orlando, FL.
[16] Cahill, D. G., 2004, "Analysis of Heat Flow in Layered Structures for Time-Domain Thermoreflectance," Rev. Sci. Instrum., **75**, pp. 5119–5122.
[17] Carslaw, H. S., and Jaeger, J. C., 1959, "Steady Periodic Temperature in Composite Slabs," *Conduction of Heat in Solids*, 2nd ed., Oxford University Press, New York, pp. 109–112.
[18] Feldman, A., 1999, "Algorithm for Solutions of the Thermal Diffusion Equation in a Stratified Medium With a Modulated Heating Source," High Temp. - High Press., **31**, pp. 293–298.
[19] Costescu, R. M., Wall, M. A., and Cahill, D. G., 2003, "Thermal Conductance of Epitaxial Interfaces," Phys. Rev. B, **67**, p. 054302.
[20] Chiritescu, C., Cahill, D. G., Heibeman, C., Lin, Q., Mortensen, C., Nguyen, N. T., Johnson, D., Rostek, R., and Bottner, H., 2008, "Low Thermal Conductivity in Nanoscale Layered Materials Synthesized by the Method of Modulated Elemental Reactants," J. Appl. Phys., **104**, p. 033533.
[21] Costescu, R. M., Bullen, A. J., Matamis, G., O'hara, K. E., and Cahill, D. G., 2002, "Thermal Conductivity and Sound Velocities of Hydrogen-Silsequioxane Low-k Dielectrics," Phys. Rev. B, **65**, p. 094205.
[22] Koh, Y. K., Cao, Y., Cahill, D. G., and Jena, D., 2009, "Heat-Transport Mechanisms in Superlattices," Adv. Funct. Mater., **19**, pp. 610–615.
[23] Hopkins, P. E., 2009, "Effects of Electron-Boundary Scattering on Changes in Thermoreflectance in Thin Metal Films Undergoing Intraband Transitions," J. Appl. Phys., **105**, p. 093517.
[24] Ezzahri, Y., Grauby, S., Dilhaire, S., Rampnoux, J. M., and Claeys, W., 2007, "Cross-Plan Si/SiGe Superlattice Acoustic and Thermal Properties Measurement by Picosecond Ultrasonics," J. Appl. Phys., **101**, p. 013705.
[25] Cahill, D. G., Ford, W. K., Goodson, K. E., Mahan, G. D., Majumdar, A., Maris, H. J., Merlin, R., and Phillpot, S. R., 2003, "Nanoscale Thermal Transport," J. Appl. Phys., **93**, pp. 793–818.
[26] Cahill, D. G., Goodson, K. E., and Majumdar, A., 2002, "Thermometry and

Thermal Transport in Micro/Nanoscale Solid-State Devices and Structures," ASME J. Heat Transfer, **124**, pp. 223–241.

[27] Stevens, R. J., Smith, A. N., and Norris, P. M., 2006, "Signal Analysis and Characterization of Experimental Setup for the Transient Thermoreflectance Technique," Rev. Sci. Instrum., **77**, p. 084901.

[28] Schmidt, A. J., 2008, "Optical Characterization of Thermal Transport From the Nanoscale to the Macroscale," Ph.D. thesis, Massachusetts Institute of Technology, Cambridge, MA.

[29] Schmidt, A. J., Cheaito, R., and Chiesa, M., 2009, "A Frequency-Domain Thermoreflectance Method for the Characterization of Thermal Properties," Rev. Sci. Instrum., **80**, p. 094901.

[30] Lee, S.-M., and Cahill, D. G., 1997, "Heat Transport in Thin Dielectric Films," J. Appl. Phys., **81**, pp. 2590–2595.

[31] Incropera, F., and Dewitt, D. P., 1996, *Fundamentals of Heat and Mass Transfer*, Wiley, New York.

[32] Norris, P. M., and Hopkins, P. E., 2009, "Examining Interfacial Diffuse Phonon Scattering Through Transient Thermoreflectance Measurements of Thermal Boundary Conductance," ASME J. Heat Transfer, **131**, p. 043207.